Structural incorporation of sorbed molybdate during iron(II)-induced transformation of ferrihydrite and goethite under advective flow conditions

Valerie A. Schoepfer [*†], Kaixuan Qin[†], Jared M. Robertson[‡], Soumya Das[†], Matthew B. J. Lindsay[*†]

[†]*Department of Geological Sciences, University of Saskatchewan, Saskatoon, SK, S7N 5E2, Canada*

[‡]*Okane Consultants Inc., Saskatoon, Saskatchewan, Canada S7N 3R3*

[*] Corresponding Authors: Tel: +1 306 966 5693.

E-mail addresses: valerie.schoepfer@usask.ca (V.A. Schoepfer); matt.lindsay@usask.ca (M.B.J. Lindsay)

Keywords: molybdenum; ferrihydrite; goethite; ferrous iron; recrystallization; lepidocrocite

ABSTRACT:

Aqueous Fe(II) can induce recrystallization of ferrihydrite and goethite [α-FeOOH] to their more crystalline or molecularly homogenous counterparts. Despite common association with these and other Fe(III) (oxyhydr)oxides, relationships between Fe(II)-induced transformation and Mo mobility remain poorly constrained. We conducted laboratory column experiments to examine repartitioning of sorbed Mo during Fe(II)-induced transformation of ferrihydrite and goethite under advective flow conditions. We first pumped ($\sim$0.25 L d^{-1}) artificial groundwater containing 0.1 mM MoO$_4^{2-}$ and buffered to pH 6.5 through columns packed with ferrihydrite- and goethite-coated sand until > 90 % Mo breakthrough was observed. Extended X-ray absorption fine structure (EXAFS) spectroscopy shows that initial MoO$_4^{2-}$ attenuation resulted from inner sphere complexation of MoO$_4$ tetrahedra at ferrihydrite and goethite surfaces. We then pumped Mo-free anoxic artificial groundwater containing 0.2 mM or 2.0 mM Fe(II) through the columns until effluent Mo concentrations remained < 0.005 mM. Raman spectroscopy shows that Fe(II) introduction induced transformation of both ferrihydrite and goethite to lepidocrocite. Additionally, Fe(II) introduction mobilized 4 to 34 % of sorbed Mo and total mass release was greater for (i) ferrihydrite compared to goethite columns and (ii) low Fe(II) compared to high Fe(II) influent. Effluent pH decreased to $\sim$5.8 for columns receiving the high Fe(II) influent and returned to pH 6.5 after 5 to 10 pore volumes. EXAFS spectroscopy indicates that structural incorporation of MoO$_6$ octahedra into neoformed phases contributes to Mo retention during Fe(II) induced transformation. Our results offer new insight into Mo repartitioning during Fe(II)-induced transformation of Fe(III) (oxyhydr)oxides and, more generally, controls on Mo mobility in geohydrologic systems.

INTRODUCTION

Molybdenum (Mo) is an oxyanion-forming metal that typically occurs at aqueous concentrations below 10 µg L^{-1} (0.0001 mM) in surface and ground waters.[1–3] Substantially higher concentrations may occur in mineralized terranes, where aqueous Mo concentrations up to 5 mg L^{-1} (0.05 mM) have been reported.[3,4] Similarly high Mo concentrations can occur in surface and ground waters impacted by industrial activities including steel manufacturing, oil refining, and chemical processing.[2,5–7] Although exposure to high Mo concentrations can have negative effects on human and plant health,[2,3] Mo also supports key biological functions in both prokaryotes and eukaryotes.[8] As a result, Mo geochemistry has implications for both origin-of-life[3] and associated paleoredox studies.[3,9–11]

Molybdenum distribution, mobility, and bioavailability in soils, sediments, and aquifers are strongly controlled by (oxyhydr)oxide and sulfide mineral occurrence and reactivity.[12,13] Sorption onto Fe(III) (oxyhydr)oxides is an important attenuation mechanism for molybdate (MoO_4^{2-}) in oxic environments.[1,14–1719] Extensive sorption of MoO_4^{2-}, AsO_4^{3-} and other metal(loid) oxyanions is favored when solution pH is less than the pH point of zero charge (pH$_{pzc}$) for Fe(III) (oxyhydr)oxides (i.e. 7.5 to 9.2).[18–21] These phases exhibit varied crystallinity ranging from poorly crystalline ferrihydrite (Fh) [hydrous Fe(III) (oxyhydr)oxide][22,23] through to more crystalline phases including the thermodynamically metastable lepidocrocite [γ-FeOOH], and the more thermodynamically stable goethite (Gt) [α-FeOOH], hematite [α-Fe$_2$O$_3$], and magnetite [Fe$_3$O$_4$].[20,24]

Soil redox oscillations occur frequently in Fe rich environments, including soils in coastal or riverine floodplains,[25] tropical or volcanic soils,[26,27] mining environments,[28,29] or anywhere water ponding occurs, including wetlands.[30] As a result, Fe (oxyhydr)oxides are often metastable near

Earth's surface.[20] Under anoxic conditions, Fe(III) (oxyhydr)oxides that exhibit poorly crystalline structures (e.g., ferrihydrite) or small crystallite sizes (i.e., high specific surface area) are particularly susceptible to reductive dissolution and transformation.[31–33] Aqueous Fe(II) is generated through partial or complete dissolution of metastable phases during microbial Fe(III) reduction.[34,35] Sorption of this aqueous Fe(II) can facilitate electron transfer and induce transformation of poorly crystalline Fe(III) (oxyhydr)oxides to more thermodynamically stable phases including goethite or magnetite through a dissolution and reprecipitation pathway.[36,37] Crystalline phases including goethite can undergo recrystallization resulting in crystallite growth without a corresponding phase transformation.[38–40] Hydrolysis of Fe(III) produced during sorbed Fe(II) electron transfer promotes precipitation and growth of (oxyhydr)oxide crystallites, while the newly formed Fe(II) can induce electron transfer at a new Fe(III) surface site.[40] The reaction rate decreases as crystallite size increases due to declining surface area[37,40] and changing redox potentials of the neoformed species.[41]

Adsorbed metals, metalloids or other elements such as As,[42,43] P,[44–46] and Mo[42,47] add an additional layer of complexity to Fe(II)-induced Fe(III) (oxyhydr)oxide transformations. Our current understanding of the fate of associated Mo during this transformation process is limited, despite the abundance of Mo in some Fe(III) (oxyhydr)oxide rich environments including those impacted by mining activities.[3,7,48] Previous studies have investigated ferrihydrite transformation under alkaline conditions (pH 8 and 10)[49,50] and elevated temperatures (75 °C).[50] These studies were conducted both with Fe(II)[49] and without Fe(II)[50], and are not broadly applicable.

Here, we describe results of laboratory columns experiments designed to examine the fate of sorbed Mo(VI) during Fe(II)-induced transformation of ferrihydrite and goethite under advective flow conditions. We hypothesize that Fe(II) induced transformation of ferrihydrite and goethite

will promote structural incorporation of adsorbed Mo into neoformed phases at circumneutral pH.[47,49,50] These experiments integrate X-ray absorption spectroscopy (XAS) and Raman spectroscopy to identify Mo bonding mechanisms and determine Fe(III) (oxyhydr)oxide phase changes. The results of our study improve understanding of geochemical controls on Mo mobility in soils, sediments, and aquifers susceptible to redox transitions.

METHODS

Preparation of Fe-coated sand

Ferrihydrite was synthesized by titration following the method of Schwertmann and Cornell.[51] Briefly, 500 mL of a 0.2 M $FeCl_3$ solution was titrated with 330 mL of a 1 N KOH solution to a pH of 7.5 while continuously stirring. The resulting precipitate was rinsed three times with deionized (DI) water, producing a 400 mL suspension that then was combined with 250 g acid washed sand (20-40 mesh Ottawa sand) in 1 L glass media bottles and shaken for 24 h. The resulting ferrihydrite-coated sand was then rinsed with DI water until the water ran clear. Excess water was removed by vacuum filtration and the coated sand was freeze dried for 24 h to inhibit crystallization. Freeze drying liberated some loosely-attached ferrihydrite; therefore, the coated sand was again rinsed, vacuum filtered, and freeze dried prior to use in the experiments. The final ferrihydrite-coated sand contained approximately 46 mmol Fe kg^{-1}. X-ray diffraction (XRD) and Raman spectroscopy of precipitates collected before sand coating confirmed the method produced 2-line ferrihydrite (Figure S1).

Goethite was synthesized by rapidly mixing 90 mL of a 5 N KOH solution with 150 mL of a 1 M $Fe(NO_3)_3 \cdot 9H_2O$ solution in a molar ratio of 9:5. The suspension was diluted to 1 L and stirred for 1 h, followed by incubation at 60 °C for 60 h to transform the precursor ferrihydrite to goethite.[51] The supernatant was decanted and the slurry was adjusted to pH 7.0 with HCl and rinsed

three times with DI water. The resulting precipitate was added to 200 g of acid-washed sand and shaken for 48 h. The sand was then rinsed until the DI water ran clear and was then freeze dried. The final goethite-coated sand contained approximately 57 mmol Fe kg^{-1}. Mineral identity was confirmed by XRD and Raman spectroscopy on precipitates collected prior to sand coating. Minor ferrihydrite was present in the synthesized goethite.

Column setup

Acid washed glass columns (Chromaflex, Kimble Chase, USA) measuring 30 cm long with an inner diameter of 4.8 cm were packed with either ferrihydrite- or goethite-coated sand to examine MoO_4^{2-} mobility during sorption and Fe(II)-induced transformations (Figure S2). This experimental setup, which included three columns containing each of ferrihydrite- and goethite-coated sand, ensured sufficient permeability to facilitate advective flow and is consistent with previous studies.[34,45,52] Approximately 23 cm of coated sand (~700 g) was packed between two 3.5 cm layers of acid-washed, non-coated Ottawa sand (~200 g). The columns were then sealed with polyfluorotetraethylene (PTFE) end fittings and high-density polyethylene (HDPE) bed supports. The bottom end fitting was connected with PTFE tubing to a low-flow multichannel peristaltic cassette pump (205CA, Watson-Marlow, USA). Approximately 0.25 L d^{-1} of influent were continuously pumped through the columns in an upward direction. The top end fitting was connected with PTFE tubing to a sealed 0.10 L amber glass flow-through cell with ports to facilitate collection of column effluent samples. Overflow from these cells subsequently flowed into 1 L HDPE bottles that were weighed frequently to track discharge volumes. Columns and tubing were wrapped with aluminum foil to exclude light. Prior to initiating the experiments, all columns were flushed with $CO_{2(g)}$ for 24 hours[53] and then saturated with Mo-free artificial groundwater (Table S1) adjusted to pH 6.5 in the presence of 10 mM PIPES buffer. This buffer

was selected because it has minimal impact on metal sorption.[54] Column pore volumes (PVs) were determined gravimetrically as the difference between the water unsaturated and saturated column masses (Table S2).

Sorption and transformation experiments

Following initial water saturation, the influent composition was systematically varied to facilitate two experimental phases: (Phase I) Mo(VI) sorption; and (Phase II) Fe(II)-induced transformations. For Phase I, 0.1 mM Mo(VI) was added to the influent by dissolving $Na_2MoO_4 \cdot 2H_2O$ ($\geq$ 99.5%, Sigma-Aldrich, USA) in the artificial groundwater. This Mo concentration was chosen based on previous studies and to mimic concentrations previously reported for mine waters,[7] while also minimizing potential for the formation of aqueous polynuclear Mo species at concentrations > 1 mM.[55] During Phase I, transport parameters were determined by adding 0.8 mM NaBr ($\geq$ 99.0%, Sigma-Aldrich, USA) to the Mo-bearing artificial groundwater and sampling effluent at 2 to 4 h intervals over three days (Supporting information). The sealed columns were located on a laboratory bench under ambient conditions (i.e., $T = 23 \pm 2$ °C, $pO_2 = 0.21$ atm) during Phase I. The Mo-bearing influent was pumped (~0.25 L d^{-1}) through the six columns until > 90% Mo breakthrough was observed. This breakthrough threshold was observed after ~120 and ~70 d for the ferrihydrite and goethite columns, respectively. The discrepancy between breakthrough times is attributed to differences in Mo sorption capacity between the ferrihydrite and goethite columns, plus minor differences in saturated hydraulic conductivity. One column containing ferrihydrite-coated sand (Fh-X) and one containing goethite-coated sand (Gt-X) was destructively sampled at the conclusion of Phase I.

The remaining four columns–two each for ferrihydrite and goethite–were transferred to an anaerobic chamber to initiate Phase II (Coy Laboratory Products). Separate influents containing

0.2 or 2 mM Fe(II) were prepared by dissolving $FeSO_4 \cdot 7H_2O$ (≥ 99.5%, Sigma-Aldrich, USA) in Mo-free artificial groundwater that was first bubbled with $N_{2(g)}$ for 24 h. The artificial groundwater composition was adjusted to avoid increasing SO_4^{2-} concentrations with $FeSO_4 \cdot 7H_2O$ addition (Table S1). The high (2.0 mM) and low (0.2 mM) Fe(II) influents were each pumped (~0.25 L d^{-1}) through one ferrihydrite and one goethite column for ~55 d until effluent Mo concentration were < 0.005 mM for all columns. The two high-Fe(II) columns (Fh-H, Gt-H) and two low-Fe(II) columns (Fh-L, Gt-L) were destructively sampled at the conclusion of Phase II.

Collection and analysis of aqueous-phase samples

Influent and effluent for each column were sampled regularly using sterile polyethylene syringes (Norm-Ject®, Henke-Sass, Wolf GmbH, Germany). Measurements of pH and redox podential (Eh) were performed immediately on unfiltered samples. The pH meter (Orion 8156 Ross Ultra, Thermo Fisher Scientific, USA) was calibrated to NIST traceable pH 4, 7 and 10 buffers, and checked against the pH 7 buffer before each measurement. Redox potential was measured using a combination Pt electrode (Orion 9678 Combination Pt Electrode, Thermo Fisher Scientific, USA) and measured values were corrected to the standard hydrogen electrode. Zobell's and Light's solutions (Ricca Chemical Co., USA) were used to regularly test Eh electrode performance.

Additional sample was passed through 0.2 μm polyethersulfone (PES) syringe filter membranes (Sartorius AG, Germany). Alkalinity was determined by titrating a known volume of filtered sample with 1.6 N H_2SO_4 (Hach Co., USA) to the bromocresol green-methyl red (Ricca Chemical Co., USA) endpoint (i.e., 4.5). Aqueous Cl$^-$ and SO_4^{2-} were quantified by ion chromatography (ICS 2100, Thermo Dionex, USA) on samples stored at 4 °C in HDPE bottles. Total aqueous Fe and Mo concentrations were determined by inductively coupled plasma-optical emission

spectroscopy (ICP-OES) and inductively coupled plasma-mass spectrometry (ICP-MS) on samples acidified to pH < 2 with concentrated high-purity HNO_3 (OmniTrace, EMD Millipore, USA) and stored at 4 °C in HDPE bottles. The aqueous Fe(II) concentrations during Phase II were analyzed by the Ferrozine spectrophotometric method while Fe_{tot} was determined by ICP-OES.[56] Samples for Ferrozine analysis were preserved with concentrated high-purity HCl (OmniTrace, EMD Millipore, USA) and diluted with $N_{2(g)}$-purged ultrapure water (> 18.18 MΩ cm) to within the range of Fe(II) standards (100 to 1000 ppb).

Collection and analysis of solid-phase samples

Prior to destructive sampling, pumping was terminated and the columns were inverted and allowed to gravity drain. Solids were collected at 2 cm intervals along the column length. These samples were transferred into 50 mL polypropylene centrifuge tubes (Falcon, Corning, USA) using clean plastic scoopulas. Samples from the Phase I only columns were air dried under ambient laboratory conditions. Samples from the Phase II columns were collected and sealed in amber glass vials within the glove box. These samples were removed from the glove box and immediately flash frozen by submerging the sealed vials in liquid N_2. All samples were then freeze dried (−50 °C) and transferred back into the glove box, where they were stored in amber glass vials in a desiccator until analysis. Solid-phase Mo and Fe contents were determined at 6 or 7 length intervals for each column by adding 2 g of Fe-coated sand to 20 mL of concentrated high-purity HCl (OmniTrace, EMD Millipore, USA) followed by ICP-OES analysis of filtered (0.45 μm PES) supernatant.

Raman spectra were obtained for hematite, lepidocrocite and magnetite[57] (Table S3), as well as obtained for synthesized ferrihydrite and goethite, and samples collected following Phase I and II. Acid-washed Ottawa sand was used as the quartz [SiO_2] reference. Iron (oxyhydr)oxide reference phases were ground using an agate mortar and pestle before mounting on a borosilicate glass slide

9

wrapped with Al foil, whereas the quartz reference and column samples were mounted directly onto the slides. The Raman microscope (Invia Reflex, Renishaw plc, UK) used a solid state laser diode operating a 785 nm lens and at 1200 line mm^{-1} (633/780) grating. A laser power of 0.1–1% was chosen for all samples to minimize any laser-induced transformation and fluorescence. The Raman microscope was calibrated to a silicon standard at 520 cm^{-1} before sample analysis. Extended scans (100–1200 cm^{-1}) were collected using the 50× objective for 30 accumulations to reduce noise.

Molybdenum K-edge X-ray absorption spectroscopy (XAS) was performed at the Hard X-ray Micro-Analysis (HXMA) beamline (06-ID-1) at the Canadian Light Source. The second of two Si(220) monochromator crystals was detuned by 50% to reject harmonics from the X-ray beam. Samples (~0.2 g) collected 5 to 7 cm from the column inlet were packed into 1.5-mm thick PTFE sample holders between two layers of polyimide adhesive tape. Reference materials were diluted in BN, homogenized using an agate mortar and pestle, and packed into the PTFE sample holders. The reference materials included MoO_3 (Sigma-Aldrich, USA), to approximate MoO_6 octahedra, plus MoO_4^{2-} sorbed onto synthetic ferrihydrite and goethite surfaces. The sample holders were positioned between ion chambers I_0 and I_1, and 10-µm thick Mo calibration foil was positioned downstream between ion chambers I_1 and I_2. The incident X-ray energy was scanned from −200 eV below the theoretical Mo K-edge (20,000 eV) to k = 14 $Å^{-1}$ at steps of 0.25 eV in the X-ray near edge spectroscopy (XANES) region and 0.05 $Å^{-1}$ in the extended X-ray absorption fine structure (EXAFS) region. Spectra were collected under ambient temperature and pressure conditions. The reference spectra were collected in transmission mode, whereas sample spectra were measured in fluorescence mode using a 32-element Ge detector (Canberra Industries Inc., USA) fitted with a Zr-filter and Soller slits. Three to five spectra were collected for each sample

to enhance the signal to noise ratio. Data reduction and analysis was performed using ATHENA and ARTEMIS (Demeter v.0.9.25).[58] Phase and amplitude functions for Mo-O, Mo-Fe, and Mo-Mo scattering paths were extracted from the crystal structures of $Fe_2(MoO_4)_3$ and molybdite using FEFF 6.0. These functions were used for non-linear least-squares fitting of the background subtracted, k^3-weighted Fourier transformed EXAFS. The Fourier transform was applied from k = 2.0 to 11.0 Å^{-1}.

Crystal morphology in samples collected from the Phase I and Phase II columns was examined using field emission – scanning electron microscope (FE-SEM; SU8010, Hitachi, Japan). Samples were mounted with carbon adhesive tape to Al stubs within the glove box, where they were transferred to a vacuum desiccator. The desiccator was transported to the FE-SEM lab where the samples were quickly transferred to a magnetron sputtering coater (Q150T SE, Quorum Technologies Ltd., UK) where a 10-nm thick Au coating was applied at low temperature to ensure sample conductance. Images were obtained using a 5 kV accelerating voltage using a backscattered electrons (BSE) detector.

Geochemical modeling

We performed thermodynamic modeling of column effluent using PHREEQCI (Version 3.4.0.12927)[59] with the integrated minteq.v4 database. Modeled saturation indices (SIs) for relevant phases including ferrihydrite, goethite, lepidocrocite and $FeMoO_4$ supported data interpretation. We input non-detect effluent Fe and Mo concentrations as one-half of the method detection limits to ensure SIs were calculated for each sampling time. Aqueous Fe speciation was simulated using the Nernst equation and input pe and total Fe values. However, previous studies have reported issues with Eh measurements in the presence of organic buffers[60] and the Ferrozine method detection limit (i.e., 0.3 μM) is above anticipated effluent Fe(III) concentrations during

Phase II.[61] Consequently, we modified Eh for consistency with reported values for Fe(II) oxidation coupled with Fe(III) (oxyhydr)oxide reduction.[41,62] Finally, we performed a sensitivity analysis of Eh values (range 0 to -300 mV) and found that associated variations in modeled SIs did not strongly affect data interpretations.

RESULTS

Aqueous chemistry

Influent and effluent pH for both the ferrihydrite and goethite columns (Figure 1a-d) was consistently circumneutral (6.55 ± 0.05) during Phase I (sorption). Influent alkalinity was approximately 1.9 mM, whereas effluent alkalinity remained between 1.8 and 2.2 mM (CaCO$_3$ eq.). Effluent Mo concentrations were initially below the ICP-MS method detection limit (0.05 µM) during Phase I, but increased to ~0.1 mM over time (Figure 2). Molybdenum was first detected (i.e., $C/C_0 > 0.05$) in effluent from the ferrihydrite and goethite columns after approximately 90 and 25 PV, respectively. Effluent Mo concentrations from the ferrihydrite columns increased to 0.09 mM (i.e., $C/C_0 = 0.90$) after 109 PV (Fh-L) and 111 PV (Fh-H). This breakthrough threshold was reached for the goethite columns after 29 PV (Gt-L) and 36 PV (Gt-H).

Phase II (reduction) was initiated at ~121 PV and ~117 PV in the ferrihydrite and goethite columns respectively. Reaction times differed between columns due to slight differences in column transport characteristics. During Phase II, influent and effluent pH were generally consistent for the low-Fe(II) columns (Fh-L, Gt-L) (Figure 1). In contrast, effluent pH initially decreased to 5.8 for both high-Fe(II) columns, but subsequently increased back to influent value of 6.5 after 130 PV (Fh-H) and 141 PV (Gt-H). Despite limited pH variability, effluent alkalinity for columns Fh-L and Gt-L ranged from 1.8 to 2.2 mM (as CaCO$_3$) following Fe(II) addition but stabilized once pH returned to influent values.

All columns exhibited declining effluent Mo concentrations over time during Phase II (Figure 2). Columns Fh-H and Gt-H exhibited rapid decreases in effluent Mo concentrations following Fe(II) addition, whereas effluent Mo concentrations declined more gradually in Fh-L and Gt-L. Effluent Mo concentrations decreased to < 0.005 mM after 176 PV (Fh-L) and 138 PV (Fh-H) for the ferrihydrite columns and after 137 PV (Gt-L) and 124 PV (Gt-H) for the goethite columns. Influent Fe concentrations in the low- and high-Fe(II) columns were initially 0.2 and 2 mM, respectively (Figure 3). For the low-Fe(II) columns, effluent Fe concentrations remained < 0.02 mM ($C/C_0 < 0.1$) until 138 PV (Fh-L) and 132 PV (Gt-L). These Fe concentrations subsequently increased to 0.13 mM (Fh-L) and 0.20 mM (Gt-L) over the final 35 to 40 PV of the experiment. Effluent Fe concentrations for the high-Fe(II) columns increased more rapidly with 90 % breakthrough ($C/C_0 > 0.9$) observed after 148 PV (Fh-H) and 128 PV (Gt-H).

Geochemical modeling

During Phase I, effluent from the ferrihydrite columns (Fh-L, Fh-H) was supersaturated with respect to ferrihydrite, goethite, lepidocrocite, hematite, and maghemite [γ-Fe_2O_3] (Figure S3). Effluent from the Fh-L column became undersaturated with respect to these Fe(III) (oxyhydr)oxides for the first ~20 PVs of Phase II. After ~20 PVs, effluent became supersaturated with respect to lepidocrocite, goethite and ferrous molybdate, while remaining undersaturated with respect to ferrihydrite. The effluent from the Fh-H column became undersaturated with respect to these Fe(III) (oxyhydr)oxides for several PVs, following which, goethite and lepidocrocite precipitation became thermodynamically favored once again. Ferrous molybdate was temporarily thermodynamically favored, however, precipitation became thermodynamically unfavorable after 180 PV (Fh-L) and 151 PV (Fh-H) corresponding to declining effluent Mo concentrations in the ferrihydrite columns (Figure S3).

Effluent from both goethite columns (Gt-L, Gt-H) was supersaturated with respect to hematite during Phase I, although slow transformation kinetics and low temperatures likely limit hematite precipitation.[63] The effluent was also supersaturated with respect to ferrihydrite, lepidocrocite, and goethite in Phase I (Figure S3). Following the initiation of Phase II, effluent became undersaturated with respect to these minerals for approximately 20 PVs in the Gt-L column and 5 PVs in the Gt-H column. Ferrihydrite did not become thermodynamically favorable again in either column; however, effluent from the Gt-L column became supersaturated with respect to $FeMoO_4$ for one PV at approximately 134 PVs in Phase II and from 119 PVs through the remainder of the experiment in the Gt-H column

Solids chemistry

Solids collected from columns Fh-X and Gt-X following Phase I contained 59 and 16 mmol Mo mol^{-1} Fe, respectively. These values correspond to 45 mmol Fe kg^{-1} of ferrihydrite-coated sand and 61 mmol Fe kg^{-1} of goethite-coated sand. Higher Mo retention observed for ferrihydrite columns is attributed to greater surface area compared to goethite, whereas higher Fe content of goethite-coated sand is attributed to greater coating effeciency.[50] Mass balance calculations indicate that average Mo contents for columns Fh-L (60 mmol Mo mol^{-1} Fe) and Fh-H (56 mmol Mo mol^{-1} Fe) following Phase I were similar to column Fh-X. Similarly, calculated average Mo contents for Gt-L (16 mmol Mo mol^{-1} Fe) and Gt-H (15 mmol Mo mol^{-1} Fe) at the conclusion of Phase I were consistent with column Gt-X. Overall, Mo surface loading in the ferrihydrite and goethite columns was approximately ~2.7 and ~0.9 mol Mo kg^{-1} Fe-coated sand, respectively.

Phase II solids collected from Fh-L exhibited average Mo contents of 51 ± 3.1 mmol Mo mol^{-1} Fe along the column length with a lower Mo content near the column inlet. In contrast, the Mo content of Phase II solids from Fh-H averaged 55 ± 3.5 mmol Mo mol^{-1} Fe and exhibited slightly

lower Mo contents near the column inlet. Average Mo contents for Phase II solids collected from Gt-L and Gt-H were 12 ± 0.7 and 16 ± 0.2 mmol Mo mol^{-1} Fe, respectively. Similar to Fh-L, limited variation in Mo content was observed along the length of these columns.

During Phase II, Fe(II) retention in columns Fh-L and Gt-L was 1.4 and 0.9 mmol Fe mol^{-1} Fe, respectively. For comparison, columns Fh-H and Gt-H retained 5.5 and 2.6 mmol Fe mol^{-1} Fe, respectively (Figure S4). Similar to Mo, these differences are attributed to greater surface area for ferrihydrite columns and higher Fe mass loading for the high Fe(II) influent.

Raman spectroscopy

Raman spectra for solid samples collected from the Phase I control columns (Fh-X, Gt-X) exhibited distinct peaks associated with quartz (~124, ~202, ~261, ~352 and ~461 cm^{-1})[64] (Figure 4). Peaks consistent with ferrihydrite (~368, ~508, and ~709 cm^{-1})[20,57] were also observed in spectra collected for Fh-X solids. The Gt-X spectra exhibited peaks attributed to quartz and goethite (~297 and 384 cm^{-1}).[20,57,65–67] A peak consistent with sorbed MoO_4^{2-} (~780 cm^{-1})[68,69] was also detected in spectra collected for Fh-X solids, which were characterized by a substantially higher Mo content at the conclusion of Phase I.

The dominant peak associated with lepidocrocite[57] at 284 cm^{-1} appeared in Fh-L and Fh-H solids following Phase II. Spectra obtained for Gt-L and Gt-H solids also exhibited distinct lepidocrocite peaks. The relative intensity of the lepidocrocite peak was greater for solids from the high-Fe(II) columns (Gt-H, Fh-H) compared to the low-Fe(II) columns. Additionally, peaks associated with goethite were not apparent in Fh-L or Fh-H solids.

X-ray absorption spectroscopy

Molybdenum K-edge XANES spectra (Figure 5) obtained for solids from the Phase I ferrihydrite (Fh-X) and goethite (Gt-X) columns exhibited a pronounced pre-edge peak at

20006 eV, two broad shoulders at 20023 and 20055 eV, and one broad peak at 20039 eV (Figure 5). These features are consistent with XANES spectra for the MoO_4^{2-} sorption reference and with published spectra for MoO_4 tetrahedra adsorbed onto goethite[47] and sodium molybdate.[70] Corresponding XANES spectra for Phase II ferrihydrite (Fh-L, Fh-H) and goethite (Gt-L, Gt-H) samples exhibited a suppressed pre-edge feature at 20006 eV, emergence of a broad peaks at ~20025 and 20037 eV, and a relative decrease in the broad peak at 20039 eV. These spectra are generally consistent with spectra obtained for the MoO_3 reference and with published spectra for distorted MoO_6 octahedra structurally incorporated into hematite.[51] We did not have a standard for octahedral Mo(VI) associated with Fe (oxyhydr)oxides. Nevertheless, qualitative assessment of XANES spectra suggests that Fe(II) introduction promoted shifts from adsorbed MoO_4 tetrahedra to structurally incorporated MoO_6 octahedra and EXAFS modeling supports this assessment.

Three coordination models were developed for Mo K-edge EXAFS spectra: (i) MoO_4 tetrahedra with varying proportions of inner- vs outer-sphere complexation to Fe (oxyhydr)oxides; (ii) MoO_6 octahedra surrounded by FeO_6 octahedra and potentially additional MoO_6 units; and (iii) a mix of these two models (Table 1).[47] Spectra obtained for Gt-X and Fh-X solids are best fit using Model 1 (Figure 5). The first shell, Mo-O_1, corresponds to MoO_4^{2-} and was present in both ferrihydrite and goethite. The Gt-X solids contained two Mo-Fe shells: an edge-sharing bidentate mononuclear surface complex to FeO_6 (Mo-Fe_1) and a corner sharing bidentate-binuclear surface complex to FeO_6 (Mo-Fe_2). In the Fh-X column, only the Mo-Fe_1 path was fit, possibly due to the lack of long-range order inhibiting binuclear complexation. The incomplete coordination (coordination number, CN = 0.5) suggests MoO_4^{2-} is only partially inner-sphere complexed.[16] Any outer-sphere complexation of MoO_4^{2-} is not resolvable via EXAFS.[50]

In comparison, Mo in MoO_3 is octahedrally coordinated[71] and can be used as a first shell approximation for octahedrally coordinated Mo(VI) with Fe(III) (oxyhydr)oxides. This phase exhibits a suppressed peak at 20006 eV, two broad peaks at 20025 and 20037 eV, and a broad shoulder at 20055 eV. Spectra obtained for Fh-H, Gt-L, and Gt-H and are best described by Model 2, where Mo-O_1 approximates the equatorial oxygen atoms in octahedral MoO_6 and Mo-O_2 approximates the axial oxygen atoms in octahedral MoO_6. A large increase in the coordination number of the Mo-Fe shells indicates that the MoO_6 units are surrounded by FeO_6 units by both edge- and corner-sharing linkages and incorporated into the bulk solid phase.[50] Inclusion of a Mo-Mo scattering path, representing linked MoO_6 units, drastically improved the quality of these fits. Although there was a relatively low concentration of Mo, MoO_6 dimers have been observed at similar concentrations.[47] Because Mo is initially concentrated at the surface of the minerals, Fe(II) induced transformation of the Fe oxide could create a thin film at the solid-liquid interface that is concentrated in Mo and more favorable for MoO_6 polymerization.

Model 3 was applied to the Fh-L column. This model represents a mixed or transition state between tetrahedral and octahedral Mo(VI). The presence of both coordination environments is indicated by decreased coordination numbers of the axial Mo-O shell (ideally $CN = 2$) and the surrounding Mo-Fe shell. The coordination number of the first shell equatorial Mo-O_1 was held constant to constrain for the presence of tetrahedral Mo(VI).

Scanning Electron Microscopy

Crystallite morphologies consistent with ferrihydrite, goethite, lepidocrocite and, potentially, green rust were observed during SEM examination of column solids.[20] The initial ferrihydrite-coated sand contained nano-scale ferrihydrite aggregated on quartz grains (Figure S5a). Rod

shaped goethite crystals and possibly some ferrihydrite associated with mineral synthesis were observed in samples of the initial goethite-coated sand (Figure S5d).[20,34,72–74]

During Phase II in the Fh-L column (Figure S5b), a large abundance of precipitates consistent with the ferrihydrite morphology were still present, along with some potential platy lepidocrocite.[20,75–77] The phase identified as lepidocrocite increased in abundance, along with some potential twinned goethite crystals in the Fh-H column (Figure S54c), which form correlated to synthesis conditions such as pH, temperature, or ionic strength.[78,79] The Gt-L and Gt-H column SEM images (Figures S5e, S5f) revealed more lepidocrocite than ferrihydrite. In both ferrihydrite and goethite columns, minor amounts of the suspected hexagonal and platy green rust were also observed.[20,80–83] Ferrimolybdate typically exhibits crystals 50 to 150 nm in size, which could not be discernable from ferrihydrite or goethite nano-crystals by SEM images.[68,78]

DISCUSSION

Molybdate sorption onto ferrihydrite and goethite

EXAFS modeling for Phase I samples reveal that Mo retention during Phase I resulted from inner sphere complexation of MoO_4 tetrahedra with ferrihydrite and goethite surfaces (Figure 5, Table 1).[17,47,50] Raman spectra (Figures 4a, 4b) and FE-SEM images (Figures S4a, S4d) of these solids support the interpretation that initial ferrihydrite and goethite did not undergo measurable transformation prior to Fe(II) addition. These findings are consistent with previous studies of MoO_4^{2-} sorption onto goethite, which occurs via surface complexation of MoO_4 tetrahedra at acidic to circumneutral pH.[47]

Molybdate sorption was approximately three times higher in the ferrihydrite columns compared to goethite columns. Mass balance calculations reveal that cumulative Mo sorption during Phase I averaged 0.66 mmol for the goethite columns and 2.0 mmol for the ferrihydrite columns. These

values correspond to 16 and 60 mmol Mo mol^{-1} Fe for the goethite and ferrihydrite columns, respectively, and are consistent with values determined from solid-phase analyses. Since these values correspond to over 90 % Mo breakthrough, they also serve as an estimate of MoO_4^{2-} sorption capacity under the experimental conditions (Figure 2).

Iron(III) (oxyhydr)oxides are effective MoO_4^{2-} sorbents in acidic to circumneutral environments.[17,47] Ferrihydrite, in particular, exhibits large capacity for sorption of MoO_4^{2-} and other anions at neutral to acidic pH because of its large surface area and net positive surface charge.[17,51] Lower MoO_4^{2-} sorption capacity of goethite under experimental conditions is largely attributed to lower surface area,[21] although surface complexation constants also vary between MoO_4^{2-} and ferrihydrite or goethite.[84]

Geochemical responses to Fe(II) introduction

Anoxic Fe(II)-bearing influent was introduced to the ferrihydrite and goethite columns after approximately 120 PV, which corresponded to 10 and 95 PVs after 90 % Mo breakthrough (i.e., $C/C_0 = 0.90$), respectively. Effluent pH for both Fh-H and Gt-H decreased immediately after Fe(II) introduction (Figure 1). These pH decreases may result from: (i) H$^+$ release to solution during aqueous Fe(II) sorption;[80] and (ii) hydrolysis of labile Fe(III) generated during the electron exchange process.[81] The lack of pH decreases for Fh-L and Gt-L is attributed to sufficient pH buffering for the lower influent Fe(II) concentration.

Effluent pH and alkalinity in the Fh-H and Gt-H columns returned to influent values within 13 to 24 PVs of Fe(II) introduction (~150 total PVs) to initiate Phase II (Figure 3b). This timing corresponds to effluent Fe(II) concentrations returning to the influent value and suggests that Fe(II) sorption and subsequent electron transfer became limited over time. This could result from changes

in the reactivity of ferrihydrite or goethite surfaces due to evolving thermodynamics[41] or a decrease in surface area.

Although Fe(II) retention eventually became limited, mass balance calculations revealed substantial Fe(II) retention during Phase II. Lower Fe(II) retention within the goethite columns is attributed to lower surface area,[51] whereas lower Fe(II) retention in Gt-L compared to Gt-H is attributed to the lower influent Fe(II) concentration. Previous studies have demonstrated that greater Fe(II) surface coverage, not higher Fe(II) concentrations, promotes faster and more complete electron transfer.[37,85,86] The extended duration of Phase II of our study (~55 d), in conjunction with the constant Fe(II) input over that time frame allowed for extended reaction of ferrihydrite and goethite, but the data also suggest that reactivity of the Fe phases declined due to changes in surface area or mineralogy as noted in the observed decrease in Fe(II) retention over time. As such, ferrihydrite and goethite transformation by the end of the experiment is suggested by the apparent lack of Raman bands associated with these phases (Figure 4). Corresponding SEM images support the interpretation that transformation of ferrihydrite and goethite was induced by Fe(II) introduction (Figure S5). Furthermore, the precipitation of lepidocrocite in the goethite columns is suspected to be a result of oxidation and precipitation of dissolved Fe(II).

Molybdenum mobilization during Fe(II) introduction

Initial Mo mobilization during Phase II is attributed to ferrihydrite and goethite dissolution due to electron transfer between sorbed Fe(II) and structural Fe(III) (Figure 5, Table 1).[87] However, longer-term Mo release was dependent on both influent Fe(II) concentration and the initial Fe(III) (oxyhydr)oxide phase (Figure 2a-d). Cumulative Mo mass discharge from ferrihydrite columns over 61 PVs during Phase II was 0.38 mmol for Fh-L and 0.09 mmol for Fh-H (Figure 2a). These values correspond to mobilization of 19 and 4.3 % of sorbed Mo(VI) during Phase I for the Fh-L

and Fh-H columns, respectively. Corresponding Mo mass discharge from goethite columns was 0.23 mmol for Gt-L and 0.06 mmol for Gt-H, which represents 34% and 8.5% of sorbed Mo(VI), respectively (Figure 2d).

Columns receiving the high Fe(II) influent exhibited lower cumulative Mo discharge compared to those receiving the low Fe(II) influent (Figure 2b and d). Greater Fe(II) availability enhances the rate and extent of Fe(III) (oxyhydr)oxide transformation[88] and neoformed phases typically exhibit lower surface area than their precursor phases.[89] Although declining surface area may explain Mo mobilization during transformation, cumulative Mo mass discharge was not proportional to influent Fe(II) concentration. Instead, cumulative Mo discharge was lower for columns receiving the high Fe(II) influent. The Fe(III) recrystallization rate is dependent on both Fe(II) concentration[36] and mineral species.[41] Advective flow therefore, may further limit Mo retention at lower Fe(III) recrystallization rates, as recrystallization reaction kinetics may be slower than column residence times.

Molybdenum repartitioning during phase transformations

A change in Mo coordination from tetrahedral to octahedral was apparent in all columns following Fe(II) addition (Figure 5a and b). Molybdenum incorporation into the solid phase is evident due to the apparent surrounding of MoO_6 octahedra by FeO_6 octahedra (Table 1). We interpret the apparent Mo incorporation in all columns as occurring during Fe(II)-induced mineral transformation. Coordination changes can result from decreasing pH,[3,47] reduction,[7] or polymerization.[90] Effluent pH did not decrease in Fh-L or Gt-L columns, but local pH decreases cannot be ruled out, as equilibrium between tetrahedral and octahedral coordinated Mo(VI) occurs at pH 4 under oxic conditions and increases to pH 6 under anoxic conditions.[3] Additionally, XAS data may provide evidence of Mo(VI) reduction or polymerization through

the presence of Mo octahedra. Molybdenum EXAFS modeling suggested Mo was coordinated with up to 2.6 edge-sharing and 5.2 corner-sharing FeO_6 units, respectively, indicating incorporation of distorted MoO_6 octahedra (Table 1). Our findings are consistent with previous results, which state that Mo(VI) may favor octahedral coordination, specifically when surrounded by FeO_6 octahedra.[50]

Molybdenum(VI) in both tetrahedral and octahedral coordination were observed in the Fh-L column whereas retained Mo(VI) within Fh-H occurred primarily in octahedral coordination (Figure 5). A greater degree of octahedral Mo(VI) coordination was observed in Gt-L. This same influent concentration resulted in higher loading to the mineral surface in the Fh-L column but could only account for partial Mo(VI) octahedra presence. We attribute this to the greater surface area of ferrihydrite, resulting in a greater Mo(VI) loading, and therefore a lower percent Fe(II) surface coverage on the Fh-L column when compared to the Gt-L column.

Peaks associated with goethite were not prominent in Raman spectra collected for Phase II samples from any column (Figures 4b, Table S3). Instead, lepidocrocite was the only Fe(III) (oxyhydr)oxide phase detected in both the ferrihydrite or goethite columns (Figure 4b).[36] Lower Fe(II) concentrations relative to previous studies[36], and consequently, fewer Fe(II) interactions with the Fe(III) (oxyhydr)oxide surface, is a potential reason for inhibited transformation of the initial minerals to crystalline secondary minerals and consequent transitory lepidocrocite abundance.[34,36,37,91] For example, previous work by Hansel et al.[34] and Boland et al.[37] describe the effect of low and high solid-associated Fe(II) on the Fe(III) (oxyhydr)oxide transformation pathway and found that, under low concentrations of solid-associated Fe(II) and pH < 6.5, lepidocrocite was the dominant transformation product.

Modeled $FeMoO_4$ saturation indices for column effluent ranged from 0.2 to 1.5 immediately following Fe(II) introduction, suggesting that precipitation of this phase was thermodynamically favorable (Figure S3). Despite the apparent supersaturation, $FeMoO_4$ was not detected by Raman (Figure 4) or EXAFS (Figure 5) spectroscopy. Although we cannot rule out the possibility of $FeMoO_4$ as a transient phase, the precipitation of $FeMoO_4$ is not a major control on Mo mobility in this study.

CONCLUSIONS AND IMPLICATIONS

Molybdenum mobilization during Fe(II)-induced Fe(III) (oxyhydr)oxide recrystallization and transformation was greater for columns containing sand coated with ferrihydrite compared to goethite. Differences between these phases are largely attributed to the higher initial adsorbed Mo mass within ferrihydrite columns prior to Fe(II) introduction. However, disparate effects of Fe(II)-induced transformation on surface area may contribute to the higher proportion of Mo mobilized during Fe(II)-induced ferrihydrite transformation. For a given initial phase, Mo mobilization was also greater for columns receiving a lower Fe(II) influent concentration. We attribute these differences to Fe(II) availability and associated differences in transformation rates. Despite these phase- and Fe(II)-dependent differences in Mo mobilization, between 66 and 96 % of adsorbed Mo was retained within the columns.

Retained Mo exhibited a distinct coordination change from MoO_4 tetrahedra to MoO_6 octahedra during Fe(II)-induced transformation. This coordination change is attributed to structural incorporation of MoO_6 octahedra into neformed lepidocrocite, which was a principal product of Fe(II)-induced ferrihydrite and goethite transformation. Our findings indicate that retention of sorbed MoO_4^{2-} during Fe(II)-induced Fe(II) (oxyhydr)oxides under advective flow conditions is

controlled by several factors. Nevertheless, substantial retention due to structural incorporation can limit Mo mobilization.

Iron (oxyhydr)oxides are an important Mo sink in Earth's crust.[3] Under anoxic conditions commonly observed in soils, sediments and aquifers[2], these phases are susceptible to reductive dissolution, which produces aqueous Fe(II) that can promote recrystallization and transformation reactions.[34] These reactions can produce more crystalline Fe (oxyhydr)oxide phases characterized by smaller surface area, leading to repartitioning of sorbed Mo between the aqueous and solid phase. Increased dissolved Mo concentrations resulting from this process, could have important water quality implications; however, structural incorporation may also limit potential for subsequent Mo release. These findings may also have implications for paleoredox studies by providing a mechanism for Mo sequestration by Fe (oxyhydr)oxides under ferruginous conditions.[93] Overall, our findings offer new insight into Mo geochemistry of soils, sediments and aquifers in both modern systems and paleoenvironments.

ASSOCIATED CONTENT

Supporting Information

The Supporting Information is available free of charge on the ACS Publications website at DOI:

Column setup, initial mineral XRD, groundwater composition, physical column parameters, details on tracer experiment, Raman reference spectra, saturation indices, SEM images, Fe(II) sorbed as a function of mineral species, and replicate Raman scans (PDF)

AUTHOR INFORMATION

ORCID

Valerie Schoepfer: 0000-0002-9582-9940

Matthew Lindsay: 0000-0001-9123-3261

Kaixuan Qin: 0000-0001-5658-1105

Jared M. Robertson: 0000-0003-2791-4438

Soumya Das: 0000-0003-1848-0164

Author Contributions

The manuscript was written through contributions of all authors. All authors have given approval to the final version of the manuscript.

Notes

The authors declare no competing financial interest.

ACKNOWLEDGEMENTS

REFERENCES

(1)   Xu, N.; Braida, W.; Christodoulatos, C.; Chen, J. A Review of Molybdenum Adsorption in Soils/Bed Sediments: Speciation, Mechanism, and Model Applications. *Soil and Sediment Contamination* **2013**, *22* (8), 912–929. https://doi.org/10.1080/15320383.2013.770438.

(2)   Smedley, P. L.; Cooper, D. M.; Ander, E. L.; Milne, C. J.; Lapworth, D. J. Occurrence of Molybdenum in British Surface Water and Groundwater: Distributions, Controls and Implications for Water Supply. *Applied Geochemistry* **2014**, *40*, 144–154. https://doi.org/10.1016/j.apgeochem.2013.03.014.

(3)   Smedley, P. L.; Kinniburgh, D. G. Molybdenum in Natural Waters: A Review of Occurrence, Distributions and Controls. *Applied Geochemistry* **2017**, *84*, 387–432. https://doi.org/10.1016/j.apgeochem.2017.05.008.

(4)   Morrison, S. J.; Mushovic, P. S.; Niesen, P. L. Early Breakthrough of Molybdenum and Uranium in a Permeable Reactive Barrier. *Environmental Science and Technology* **2006**, *40* (6), 2018–2024. https://doi.org/10.1021/es052128s.

(5)   Conlan, M. J. W.; Mayer, K. U.; Blaskovich, R.; Beckie, R. D. Solubility Controls for Molybdenum in Neutral Rock Drainage. *Geochemistry: Exploration, Environment, Analysis* **2012**, *12* (1), 21–32. https://doi.org/10.1144/1467-7873/10-ra-043.

(6)   Kargar, M.; Khorasani, N.; Karami, M.; Rafiee, G.-R.; Naseh, R. Study of Aluminum, Copper and Molybdenum Pollution in Groundwater Sources Surrounding (Miduk) Shahr-E-Babak Copper Complex Tailings Dam. *World Academy of Science, Engineering & Technology* **2011**, *52* (4), 412–416.

(7)   Robertson, J. M.; Nesbitt, J. A.; Lindsay, M. B. J. Aqueous- and Solid-Phase Molybdenum Geochemistry of Oil Sands Fluid Petroleum Coke Deposits, Alberta, Canada. *Chemosphere* **2019**, *217*, 715–723. https://doi.org/10.1016/j.chemosphere.2018.11.064.

(8)   Barceloux, D. G.; Barceloux, D. Molybdenum. *Journal of Toxicology: Clinical Toxicology* **1999**, *37* (2), 231–237. https://doi.org/10.1081/CLT-100102422.

(9)   Tribovillard, N.; Algeo, T. J.; Lyons, T.; Riboulleau, A. Trace Metals as Paleoredox and Paleoproductivity Proxies: An Update. *Chemical Geology* **2006**, *232* (1–2), 12–32. https://doi.org/10.1016/j.chemgeo.2006.02.012.

(10)   Duan, Y.; Anbar, A. D.; Arnold, G. L.; Lyons, T. W.; Gordon, G. W.; Kendall, B. Molybdenum Isotope Evidence for Mild Environmental Oxygenation before the Great Oxidation Event. *Geochimica et Cosmochimica Acta* **2010**, *74* (23), 6655–6668. https://doi.org/10.1016/j.gca.2010.08.035.

(11)   Scholz, F.; Siebert, C.; Dale, A. W.; Frank, M. Intense Molybdenum Accumulation in Sediments underneath a Nitrogenous Water Column and Implications for the Reconstruction of Paleo-Redox Conditions Based on Molybdenum Isotopes. *Geochimica et Cosmochimica Acta* **2017**, *213*, 400–417. https://doi.org/10.1016/j.gca.2017.06.048.

(12)   Pichler, T.; Mozaffari, A. Distribution and Mobility of Geogenic Molybdenum and Arsenic in a Limestone Aquifer Matrix. *Applied Geochemistry* **2015**, *63*, 623–633. https://doi.org/10.1016/j.apgeochem.2015.08.006.

(13)   Leybourne, M. I.; Cameron, E. M. Source, Transport, and Fate of Rhenium, Selenium, Molybdenum, Arsenic, and Copper in Groundwater Associated with Porphyry-Cu Deposits, Atacama Desert, Chile. *Chemical Geology* **2008**, *247* (1–2), 208–228. https://doi.org/10.1016/j.chemgeo.2007.10.017.

(14) McKenzie, R. M. The Adsorption of Molybdenum on Oxide Surfaces. *Australian Journal of Soil Research* **1983**, *21* (4), 505–513. https://doi.org/10.1071/SR9830505.

(15) LeGendre, G. R.; Runnells, D. D. Removal of Dissolved Molybdenum from Wastewaters by Precipitates of Ferric Iron. *Environmental Science and Technology* **1975**, *9* (8), 744–749. https://doi.org/10.1021/es60106a010.

(16) Gustafsson, J. P.; Tiberg, C. Molybdenum Binding to Soil Constituents in Acid Soils: An XAS and Modelling Study. *Chemical Geology* **2015**, *417*, 279–288. https://doi.org/10.1016/j.chemgeo.2015.10.016.

(17) Brinza, L.; Vu, H. P.; Neamtu, M.; Benning, L. G. Experimental and Simulation Results of the Adsorption of Mo and V onto Ferrihydrite. *Scientific Reports* **2019**, *9* (1), 1–12. https://doi.org/10.1038/s41598-018-37875-y.

(18) Li, Z.; Zhang, T.; Li, K. One-Step Synthesis of Mesoporous Two-Line Ferrihydrite for Effective Elimination of Arsenic Contaminants from Natural Water. *Dalton Trans.* **2011**, *40* (9), 2062. https://doi.org/10.1039/c0dt01138j.

(19) Brinza, L.; Benning, L. G.; Statham, P. J. Adsorption Studies of Mo and V onto Ferrihydrite. *Mineral. mag.* **2008**, *72* (1), 385–388. https://doi.org/10.1180/minmag.2008.072.1.385.

(20) Cornell, R. M.; Schwertmann, U. *The Iron Oxides: Structure, Reactions, Occurrence and Uses*, 2nd ed.; 2003.

(21) Hiemstra, T.; van Riemsdijk, W. H. Adsorption and Surface Oxidation of Fe(II) on Metal (Hydr)Oxides. *Geochimica et Cosmochimica Acta* **2007**, *71* (24), 5913–5933. https://doi.org/10.1016/j.gca.2007.09.030.

(22) Peak, D.; Regier, T. Z. Response to Comment on "Direct Observation of Tetrahedrally Coordinated Fe(III) in Ferrihydrite." *Environ. Sci. Technol.* **2012**, *46* (12), 6885–6887. https://doi.org/10.1021/es302143n.

(23) Peak, D.; Regier, T. Direct Observation of Tetrahedrally Coordinated Fe(III) in Ferrihydrite. *Environ. Sci. Technol.* **2012**, *46* (6), 3163–3168. https://doi.org/10.1021/es203816x.

(24) Benner, S. G.; Hansel, C. M.; Wielinga, B. W.; Barber, T. M.; Fendorf, S. Reductive Dissolution and Biomineralization of Iron Hydroxide under Dynamic Flow Conditions. *Environmental Science and Technology* **2002**, *36* (8), 1705–1711. https://doi.org/10.1021/es0156441.

(25) Chen, C.; Barcellos, D.; Richter, D. D.; Schroeder, P. A.; Thompson, A. Redoximorphic Bt Horizons of the Calhoun CZO Soils Exhibit Depth-Dependent Iron-Oxide Crystallinity. *J Soils Sediments* **2019**, *19* (2), 785–797. https://doi.org/10.1007/s11368-018-2068-2.

(26) Barcellos, D.; Cyle, K. T.; Thompson, A. Faster Redox Fluctuations Can Lead to Higher Iron Reduction Rates in Humid Forest Soils. *Biogeochemistry* **2018**, *137* (3), 367–378. https://doi.org/10.1007/s10533-018-0427-0.

(27) Thompson, A.; Rancourt, D. G.; Chadwick, O. A.; Chorover, J. Iron Solid-Phase Differentiation along a Redox Gradient in Basaltic Soils. *Geochimica et Cosmochimica Acta* **2011**, *75* (1), 119–133. https://doi.org/10.1016/j.gca.2010.10.005.

(28) Torres, E.; Couture, R. M.; Shafei, B.; Nardi, A.; Ayora, C.; Van Cappellen, P. Reactive Transport Modeling of Early Diagenesis in a Reservoir Lake Affected by Acid Mine Drainage: Trace Metals, Lake Overturn, Benthic Fluxes and Remediation. *Chemical Geology* **2015**, *419*, 75–91. https://doi.org/10.1016/j.chemgeo.2015.10.023.

(29) Schaider, L. A.; Senn, D. B.; Estes, E. R.; Brabander, D. J.; Shine, J. P. Sources and Fates of Heavy Metals in a Mining-Impacted Stream: Temporal Variability and the Role of Iron Oxides. *Science of The Total Environment* **2014**, *490*, 456–466. https://doi.org/10.1016/j.scitotenv.2014.04.126.

(30) Koretsky, C. M.; Moore, C. M.; Meile, C.; Dichristina, T. J.; Cappellen, V. Seasonal Oscillation of Microbial Iron and Sulfate Reduction in Saltmarsh Sediments (Sapelo Island, GA, USA). 26.

(31) Roden, E. E.; Zachara, J. M. Microbial Reduction of Crystalline Iron(III) Oxides: Influence of Oxide Surface Area and Potential for Cell Growth. *Environ. Sci. Technol.* **1996**, *30* (5), 1618–1628. https://doi.org/10.1021/es9506216.

(32) Paikaray, S.; Schröder, C.; Peiffer, S. Schwertmannite Stability in Anoxic Fe(II)-Rich Aqueous Solution. *Geochimica et Cosmochimica Acta* **2017**, *217*, 292–305. https://doi.org/10.1016/j.gca.2017.08.026.

(33) Paikaray, S.; Peiffer, S. Lepidocrocite Formation Kinetics from Schwertmannite in Fe(II)-Rich Anoxic Alkaline Medium. *Mine Water Environ* **2015**, *34* (2), 213–222. https://doi.org/10.1007/s10230-014-0309-1.

(34) Hansel, C. M.; Benner, S. G.; Neiss, J.; Dohnalkova, A.; Kukkadapu, R. K.; Fendorf, S. Secondary Mineralization Pathways Induced by Dissimilatory Iron Reduction of Ferrihydrite under Advective Flow. *Geochimica et Cosmochimica Acta* **2003**, *67* (16), 2977–2992. https://doi.org/10.1016/S0016-7037(03)00276-X.

(35) Xiao, W.; Jones, A. M.; Li, X.; Collins, R. N.; Waite, T. D. Effect of *Shewanella Oneidensis* on the Kinetics of Fe(II)-Catalyzed Transformation of Ferrihydrite to Crystalline Iron Oxides. *Environ. Sci. Technol.* **2018**, *52* (1), 114–123. https://doi.org/10.1021/acs.est.7b05098.

(36) Hansel, C. M.; Benner, S. G.; Fendorf, S. Competing Fe(II)-Induced Mineralization Pathways of Ferrihydrite. *Environmental Science & Technology* **2005**, *39* (18), 7147–7153. https://doi.org/10.1021/es050666z.

(37) Boland, D. D.; Collins, R. N.; Miller, C. J.; Glover, C. J.; Waite, T. D. Effect of Solution and Solid-Phase Conditions on the Fe(II)-Accelerated Transformation of Ferrihydrite to Lepidocrocite and Goethite. *Environmental Science and Technology* **2014**, *48* (10), 5477–5485. https://doi.org/10.1021/es4043275.

(38) Handler, R. M.; Beard, B. L.; Johnson, C. M.; Scherer, M. M. Atom Exchange between Aqueous Fe(II) and Goethite: An Fe Isotope Tracer Study. *Environmental Science and Technology* **2009**, *43* (4), 1102–1107. https://doi.org/10.1021/es802402m.

(39) Handler, R. M.; Frierdich, A. J.; Johnson, C. M.; Rosso, K. M.; Brian, L.; Wang, C.; Latta, D. E.; Neumann, A.; Pasakarnis, T.; Scherer, M. M.; Beard, B. L.; Wang, C.; Latta, D. E.; Neumann, A.; Pasakarnis, T.; Premaratne, W. A. P. J.; Scherer, M. M. Fe(II)-Catalyzed Recrystallization of Goethite Revisited. *Environmental Science & Technology* **2014**, *48* (Ii), 11302–11311. https://doi.org/10.1021/es503084u.

(40) Southall, S. C.; Micklethwaite, S.; Wilson, S. A.; Frierdich, A. J. Changes in Crystallinity and Tracer-Isotope Distribution of Goethite during Fe(II)-Accelerated Recrystallization. *ACS Earth and Space Chemistry* **2018**, *2* (12), 1271–1282. https://doi.org/10.1021/acsearthspacechem.8b00100.

(41) Jones, A. M.; Collins, R. N.; Waite, T. D. Redox Characterization of the Fe(II)-Catalyzed Transformation of Ferrihydrite to Goethite. *Geochimica et Cosmochimica Acta* **2017**, *218*, 257–272. https://doi.org/10.1016/j.gca.2017.09.024.

(42) Antelo, J.; Fiol, S.; Gondar, D.; López, R.; Arce, F. Comparison of Arsenate, Chromate and Molybdate Binding on Schwertmannite: Surface Adsorption vs Anion-Exchange. *Journal of Colloid and Interface Science* **2012**, *386* (1), 338–343. https://doi.org/10.1016/j.jcis.2012.07.008.

(43) Bennett, B.; Dudas, M. J. Release of Arsenic and Molybdenum by Reductive Dissolution of Iron Oxides in a Soil with Enriched Levels of Native Arsenic. *Journal of Environmental Engineering and Science* **2003**, *2* (4), 265–272. https://doi.org/10.1139/s03-028.

(44) Abdala, D. B.; Northrup, P. A.; Arai, Y.; Sparks, D. L. Surface Loading Effects on Orthophosphate Surface Complexation at the Goethite/Water Interface as Examined by Extended X-Ray Absorption Fine Structure (EXAFS) Spectroscopy. *Journal of Colloid and Interface Science* **2015**, *437*, 297–303. https://doi.org/10.1016/j.jcis.2014.09.057.

(45) Borch, T.; Masue, Y.; Kukkadapu, R. K.; Fendorf, S. Phosphate Imposed Limitations on Biological Reduction and Alteration of Ferrihydrite. *Environ. Sci. Technol.* **2007**, *41* (1), 166–172. https://doi.org/10.1021/es060695p.

(46) Borch, T.; Fendorf, S. Chapter 12 Phosphate Interactions with Iron (Hydr)Oxides: Mineralization Pathways and Phosphorus Retention upon Bioreduction. In *Developments in Earth and Environmental Sciences*; Elsevier, 2007; Vol. 7, pp 321–348. https://doi.org/10.1016/S1571-9197(07)07012-7.

(47) Arai, Y. X-Ray Absorption Spectroscopic Investigation of Molybdenum Multinuclear Sorption Mechanism at the Goethite-Water Interface. *Environmental Science and Technology* **2010**, *44* (22), 8491–8496. https://doi.org/10.1021/es101270g.

(48) Skierszkan, E. K.; Robertson, J. M.; Lindsay, M. B. J.; Stockwell, J. S.; Dockrey, J. W.; Das, S.; Weis, D.; Beckie, R. D.; Mayer, K. U. Tracing Molybdenum Attenuation in Mining Environments Using Molybdenum Stable Isotopes. *Environ. Sci. Technol.* **2019**, *53* (10), 5678–5686. https://doi.org/10.1021/acs.est.9b00766.

(49) Gomez, M. A.; Jim Hendry, M.; Hossain, A.; Das, S.; Elouatik, S. Abiotic Reduction of 2-Line Ferrihydrite: Effects on Adsorbed Arsenate, Molybdate, and Nickel. *RSC Advances* **2013**, *3* (48), 25812–25822. https://doi.org/10.1039/c3ra44769c.

(50) Das, S.; Essilfie-Dughan, J.; Hendry, J.; Jim Hendry, M. Sequestration of Molybdate during Transformation of 2-Line Ferrihydrite under Alkaline Conditions. *Applied Geochemistry* **2016**, *73*, 70–80. https://doi.org/10.1016/j.apgeochem.2016.08.003.

(51) Schwertmann, U.; Cornell, R. M. *Iron Oxides in the Laboratory*; 1991; Vol. 2. https://doi.org/10.1180/minmag.1992.056.383.20.

(52) Hansel, C. M.; Benner, S. G.; Nico, P.; Fendorf, S. Structural Constraints of Ferric (Hydr)Oxides on Dissimilatory Iron Reduction and the Fate of Fe(II). *Geochimica et Cosmochimica Acta* **2004**, *68* (15), 3217–3229. https://doi.org/10.1016/j.gca.2003.10.041.

(53) Vessey, C. J.; Lindsay, M. B. J.; Barbour, S. L. Sodium Transport and Attenuation in Soil Cover Materials for Oil Sands Mine Reclamation. *Applied Geochemistry* **2019**, *100*, 42–54. https://doi.org/10.1016/j.apgeochem.2018.10.023.

(54) Szecsody, J. E.; Zachara, J. M.; Bruckhart, P. L. Adsorption-Dissolution Reactions Affecting the Distribution and Stability of CoII EDTA in Iron Oxide-Coated Sand. *Environmental Science and Technology* **1994**, *28* (9), 1706–1716. https://doi.org/10.1021/es00058a024.

(55) Cruywagen, J. J. PROTONAT1ON, OLIGOMERIZATlON, AND CONDENSATION REACTIONS OF VANADATE(V), MOLYBDATE(VI), AND TUNGSTATE(VI). In *Advances in Inorganic Chemistry*; Academic press, 2000; Vol. 49, p 56.

(56) Gibbs, M. M. A Simple Method for the Rapid Determination of Iron in Natural Waters. *Water Research* **1979**, *13* (3), 295–297. https://doi.org/10.1016/0043-1354(79)90209-4.

(57) Das, S.; Hendry, M. J. Application of Raman Spectroscopy to Identify Iron Minerals Commonly Found in Mine Wastes. *Chemical Geology* **2011**, *290* (3–4), 101–108. https://doi.org/10.1016/j.chemgeo.2011.09.001.

(58) Ravel, B.; Newville, M. ATHENA, ARTEMIS, HEPHAESTUS: Data Analysis for X-Ray Absorption Spectroscopy Using IFEFFIT. *Journal of Synchrotron Radiation* **2005**, *12* (4), 537–541. https://doi.org/10.1107/S0909049505012719.

(59) Parkhurst, D., L.; Appelo, C. A. J. *Description of Input and Examples for PHREEQC Version 3—A Computer Program for Speciation, Batch-Reaction, One-Dimensional Transport, and Inverse Geochemical Calculations*; Modeling Techniques; U.S. Geological Survey, 2013.

(60) Markelova, E.; Parsons, C. T.; Couture, R.-M.; Smeaton, C. M.; Madé, B.; Charlet, L.; Van Cappellen, P. Deconstructing the Redox Cascade: What Role Do Microbial Exudates (Flavins) Play? *Environ. Chem.* **2017**, *14* (8), 515. https://doi.org/10.1071/EN17158.

(61) Viollier, E.; Inglett, P. W.; Hunter, K.; Roychoudhury, A. N.; Van Cappellen, P. The Ferrozine Method Revisited: Fe(II)/Fe(III) Determination in Natural Waters. *Applied Geochemistry* **2000**, *15* (6), 785–790. https://doi.org/10.1016/S0883-2927(99)00097-9.

(62) Borch, T.; Kretzschmar, R.; Kappler, A.; Cappellen, P. V.; Ginder-Vogel, M.; Voegelin, A.; Campbell, K. Biogeochemical Redox Processes and Their Impact on Contaminant Dynamics. *Environ. Sci. Technol.* **2010**, *44* (1), 15–23. https://doi.org/10.1021/es9026248.

(63) Schwertmann, U.; Cornell, R. *Iron Oxides in the Laboratory*, 2nd ed.; Wiley: New York, 2000.

(64) Mernagh, T. P.; Liu, L. Temperature Dependence of Raman Spectra of the Quartz- and Rutile-Types of GeO 2. *Physics and Chemistry of Minerals* **1997**, *24* (1), 7–16. https://doi.org/10.1007/s002690050012.

(65) de Faria, D. L. A.; Silva, S. V.; de Oliveria, M. T. Raman Microspectroscopy of Some Iron Oxides and Oxyhydroxides. *J. Raman Spectrosc.* **1997**, *28*, 873–878.

(66) Legodi, M. A.; de Waal, D. The Preparation of Magnetite, Goethite, Hematite and Maghemite of Pigment Quality from Mill Scale Iron Waste. *Dyes and Pigments* **2006**, *74* (1), 161–168. https://doi.org/10.1016/j.dyepig.2006.01.038.

(67) Hanesch, M. Raman Spectroscopy of Iron Oxides and (Oxy)Hydroxides at Low Laser Power and Possible Applications in Environmental Magnetic Studies. *Geophysical Journal International* **2009**, *177* (3), 941–948. https://doi.org/10.1111/j.1365-246X.2009.04122.x.

(68) Routray, K.; Zhou, W.; Kiely, C. J.; Grünert, W.; Wachs, I. E. Origin of the Synergistic Interaction between MoO3 and Iron Molybdate for the Selective Oxidation of Methanol to Formaldehyde. *Journal of Catalysis* **2010**, *275* (1), 84–98. https://doi.org/10.1016/j.jcat.2010.07.023.

(69) Tian, H.; Wachs, I. E.; Briand, L. E. Comparison of UV and Visible Raman Spectroscopy of Bulk Metal Molybdate and Metal Vanadate Catalysts. *Journal of Physical Chemistry B* **2005**, *109* (49), 23491–23499. https://doi.org/10.1021/jp053879j.

(70) Wharton, J. A.; Ross, D. H.; Treacy, G. M.; Wilcox, G. D.; Baldwin, K. R. An EXAFS Investigation of Molybdate-Based Conversion Coatings. *Journal of Applied Electrochemistry* **2003**, *33*, 553–561.

(71) Wagner, M.; Chappaz, A.; Lyons, T. W. Molybdenum Speciation and Burial Pathway in Weakly Sulfidic Environments: Insights from XAFS. *Geochimica et Cosmochimica Acta* **2017**, *206*, 18–29. https://doi.org/10.1016/j.gca.2017.02.018.

(72) Xu, Y.; Axe, L. Synthesis and Characterization of Iron Oxide-Coated Silica and Its Effect on Metal Adsorption. *Journal of Colloid and Interface Science* **2005**, *282* (1), 11–19. https://doi.org/10.1016/j.jcis.2004.08.057.

(73) Rusch, B.; Hanna, K.; Humbert, B. Coating of Quartz Silica with Iron Oxides: Characterization and Surface Reactivity of Iron Coating Phases. *Colloids and Surfaces A: Physicochemical and Engineering Aspects* **2010**, *353* (2–3), 172–180. https://doi.org/10.1016/j.colsurfa.2009.11.009.

(74) Amstaetter, K.; Borch, T.; Larese-Casanova, P.; Kappler, A. Redox Transformation of Arsenic by Fe(II)-Activated Goethite (α-FeOOH). *Environ. Sci. Technol.* **2010**, *44* (1), 102–108. https://doi.org/10.1021/es901274s.

(75) Liu, H.; Ma, M.; Qin, M.; Yang, L.; Wei, Y. Journal of Solid State Chemistry Studies on the Controllable Transformation of Ferrihydrite. *Journal of Solid State Chemistry* **2010**, *183* (9), 2045–2050. https://doi.org/10.1016/j.jssc.2010.07.012.

(76) Bae, S.; Lee, W. Biotransformation of Lepidocrocite in the Presence of Quinones and Flavins. *Geochimica et Cosmochimica Acta* **2013**, *114*, 144–155. https://doi.org/10.1016/j.gca.2013.03.041.

(77) Kozin, P. A.; Salazar-Alvarez, G.; Boily, J. F. Oriented Aggregation of Lepidocrocite and Impact on Surface Charge Development. *Langmuir* **2014**, *30* (30), 9017–9021. https://doi.org/10.1021/la500507e.

(78) Cornell, R. M. M.; Schwertmann, U. *The Iron Oxides: Structure, Reactions, Occurences and Uses*, 2nd ed.; Wiley-VCH Verlag GmbH & Co. KGaA, Weinheim, 2003. https://doi.org/10.1002/3527602097.ch1.

(79) Cornell, R. M.; Giovanoli, R. Effect of Solution Conditions on the Proportion and Morphology of Goethite Formed from Ferrihydrite. *Clays and Clay Minerals* **1985**, *33* (5), 424–432. https://doi.org/10.1346/CCMN.1985.0330508.

(80) Ruby, C.; Géhin, A.; Abdelmoula, M.; Génin, J. M. R.; Jolivet, J. P. Coprecipitation of Fe(II) and Fe(III) Cations in Sulphated Aqueous Medium and Formation of Hydroxysulphate Green Rust. *Solid State Sciences* **2003**, *5* (7), 1055–1062. https://doi.org/10.1016/S1293-2558(03)00121-3.

(81) Lindsay, M. B. J.; Ptacek, C. J.; Blowes, D. W.; Gould, W. D. Zero-Valent Iron and Organic Carbon Mixtures for Remediation of Acid Mine Drainage: Batch Experiments. *Applied Geochemistry* **2008**, *23* (8), 2214–2225. https://doi.org/10.1016/j.apgeochem.2008.03.005.

(82) Kocar, B. D.; Borch, T.; Fendorf, S. Arsenic Repartitioning during Biogenic Sulfidization and Transformation of Ferrihydrite. *Geochimica et Cosmochimica Acta* **2010**, *74* (3), 980–994. https://doi.org/10.1016/j.gca.2009.10.023.

(83) Sergent, A. S.; Jorand, F.; Hanna, K. Effects of Si-Bearing Minerals on the Nature of Secondary Iron Mineral Products from Lepidocrocite Bioreduction. *Chemical Geology* **2011**, *289* (1–2), 86–97. https://doi.org/10.1016/j.chemgeo.2011.07.016.

(84)   Dzombak, D. A.; Morel, F. *Surface Complexation Modeling : Hydrous Ferric Oxide*; Wiley: New York, 1990.

(85)   Williams, A. G. B.; Scherer, M. M. Spectroscopic Evidence for Fe(II)−Fe(III) Electron Transfer at the Iron Oxide−Water Interface. *Environmental Science & Technology* **2004**, *38* (18), 4782–4790. https://doi.org/10.1021/es049373g.

(86)   Poulson, R. L. Iron Isotope Exchange Kinetics at the Nanoparticulate Ferrihydrite Surface. *American Mineralogist* **2005**, *90* (4), 758–763. https://doi.org/10.2138/am.2005.1802.

(87)   Pedersen, H. D.; Postma, D.; Jakobsen, R. Release of Arsenic Associated with the Reduction and Transformation of Iron Oxides. *Geochimica et Cosmochimica Acta* **2006**, *70* (16), 4116–4129. https://doi.org/10.1016/j.gca.2006.06.1370.

(88)   Burton, E. D.; Bush, R. T.; Sullivan, L. a.; Mitchell, D. R. G. Schwertmannite Transformation to Goethite via the Fe(II) Pathway: Reaction Rates and Implications for Iron–Sulfide Formation. *Geochimica et Cosmochimica Acta* **2008**, *72* (18), 4551–4564. https://doi.org/10.1016/j.gca.2008.06.019.

(89)   Hiemstra, T.; Mendez, J. C.; Li, J. Evolution of the Reactive Surface Area of Ferrihydrite: Time, PH, and Temperature Dependency of Growth by Ostwald Ripening. *Environ. Sci.: Nano* **2019**, *6* (3), 820–833. https://doi.org/10.1039/C8EN01198B.

(90)   Davantès, A.; Costa, D.; Sallman, B.; Rakshit, S.; Lefev, G. Surface Polymerization of Mo(VI) and W(VI) Anions on Hematite Revealed by in Situ Infrared Spectroscopy and DFT+U Theoretical Study. *J. Phys. Chem. C* **2017**, 9.

(91)   Pedersen, H. D.; Postma, D.; Jakobsen, R.; Larsen, O. Fast Transformation of Iron Oxyhydroxides by the Catalytic Action of Aqueous Fe(II). *Geochimica et Cosmochimica Acta* **2005**, *69* (16), 3967–3977. https://doi.org/10.1016/j.gca.2005.03.016.

(92)   Poulton, S. W.; Canfield, D. E. Ferruginous Conditions: A Dominant Feature of the Ocean through Earth's History. *Elements* **2011**, *7* (2), 107–112. https://doi.org/10.2113/gselements.7.2.107.
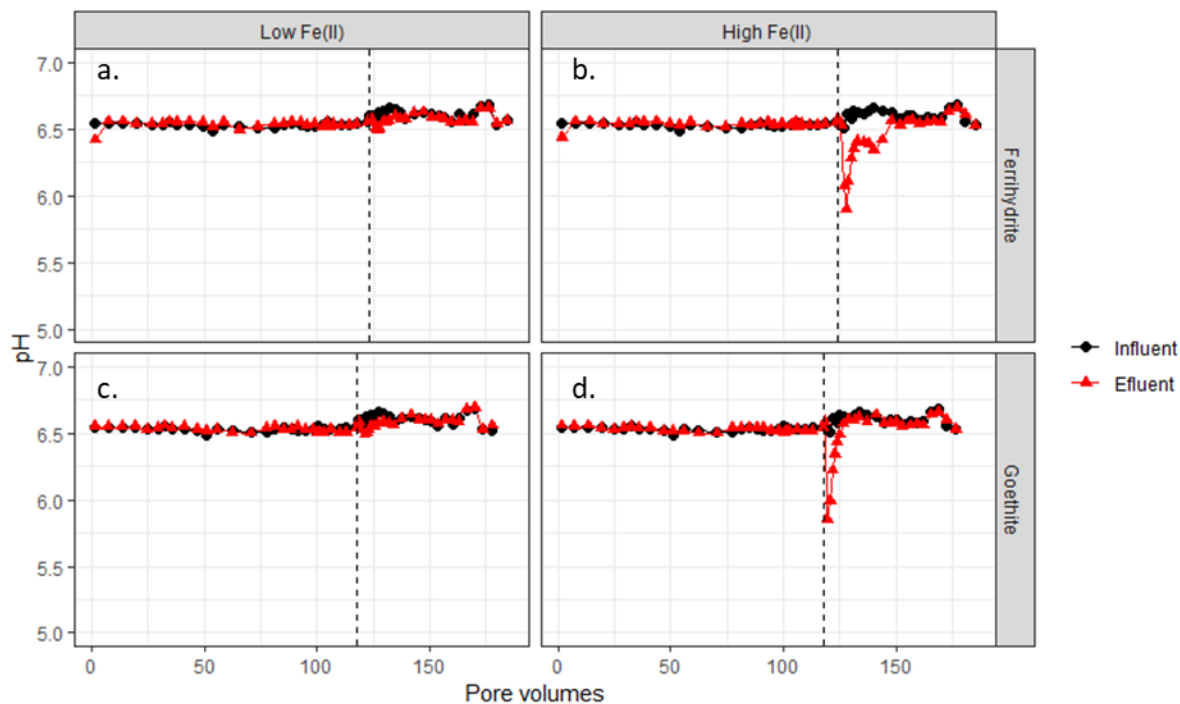
Figure 1. pH as a function of pore volume in each of the ferrihydrite (a and b) and goethite (c and d) columns before and during Fe(II) input. Black circles and red triangles represent column influent and effluent, respectively. The vertical dashed black line indicates the initiation of the reduction phase.
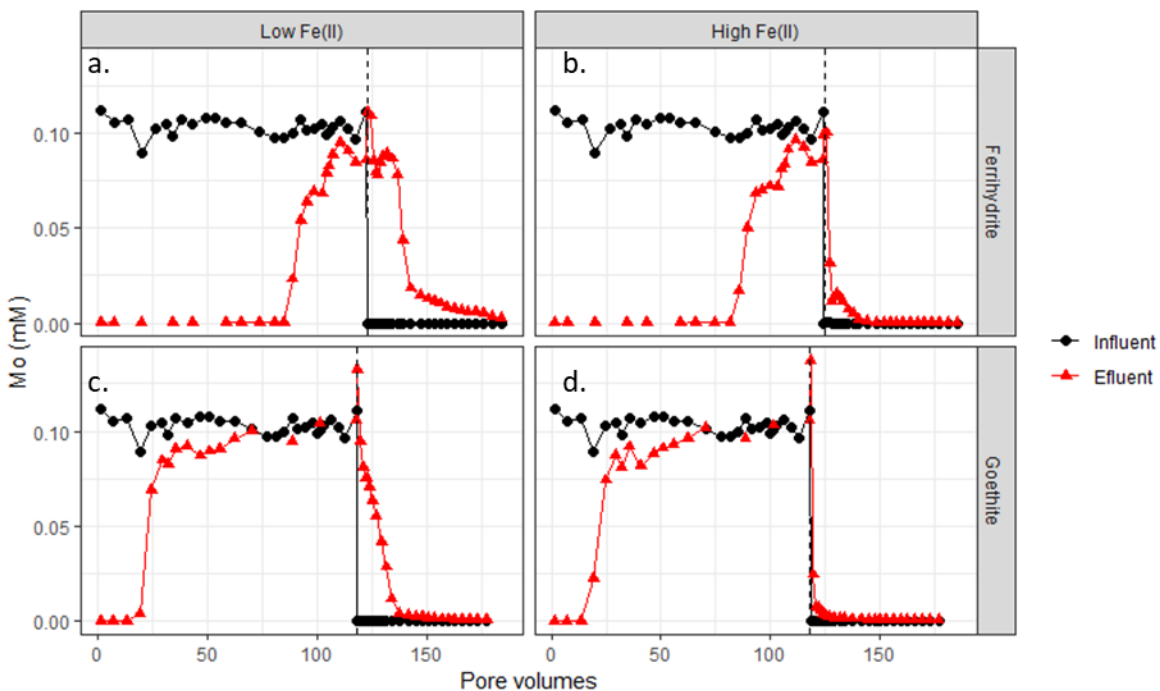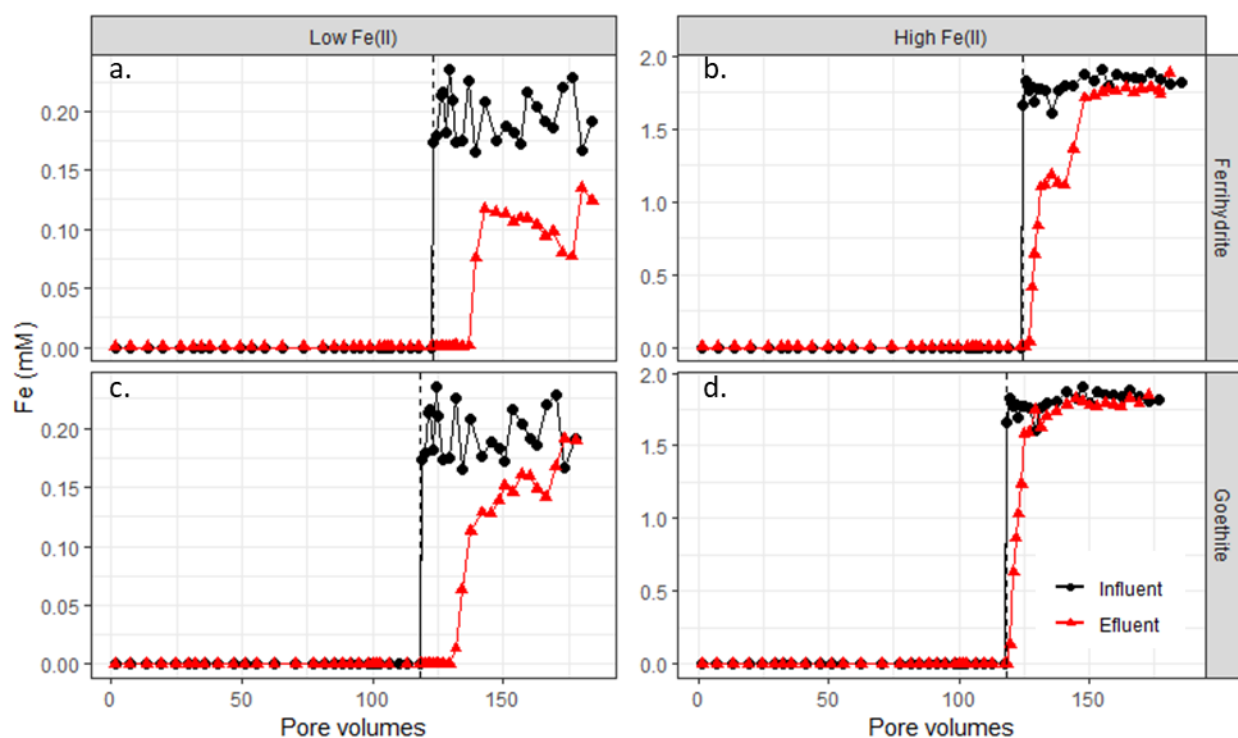
Figure 2. Molybdenum concentrations (mM) as a function of pore volume in each of the ferrihydrite (a and b) and goethite (c and d) columns before and during Fe(II) input. Black circles and red triangles represent column influent and effluent, respectively. The vertical dashed black line indicates the initiation of the reduction phase.

Figure 3. Fe(II) concentrations (mM) as a function of pore volume in each of the ferrihydrite (a and b) and goethite (c and d) columns before and during Fe(II) input. Black circles and red triangles represent column influent and effluent, respectively. The vertical dashed black line indicates the initiation of the reduction phase.
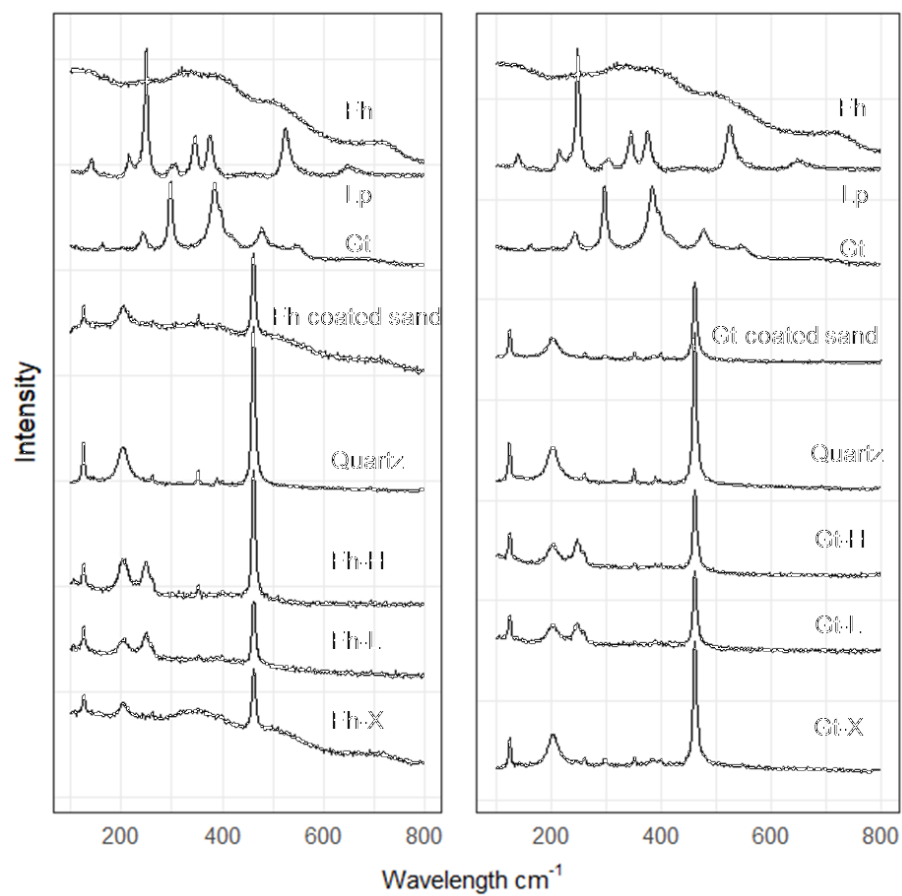
Figure 4. Raman spectra for samples collected from ferrihydrite (Fh, left panel) and goethite (Gt, right panel) columns before and after introduction of the low (0.2 mM) and high (2.0 mM) Fe(II) influents.
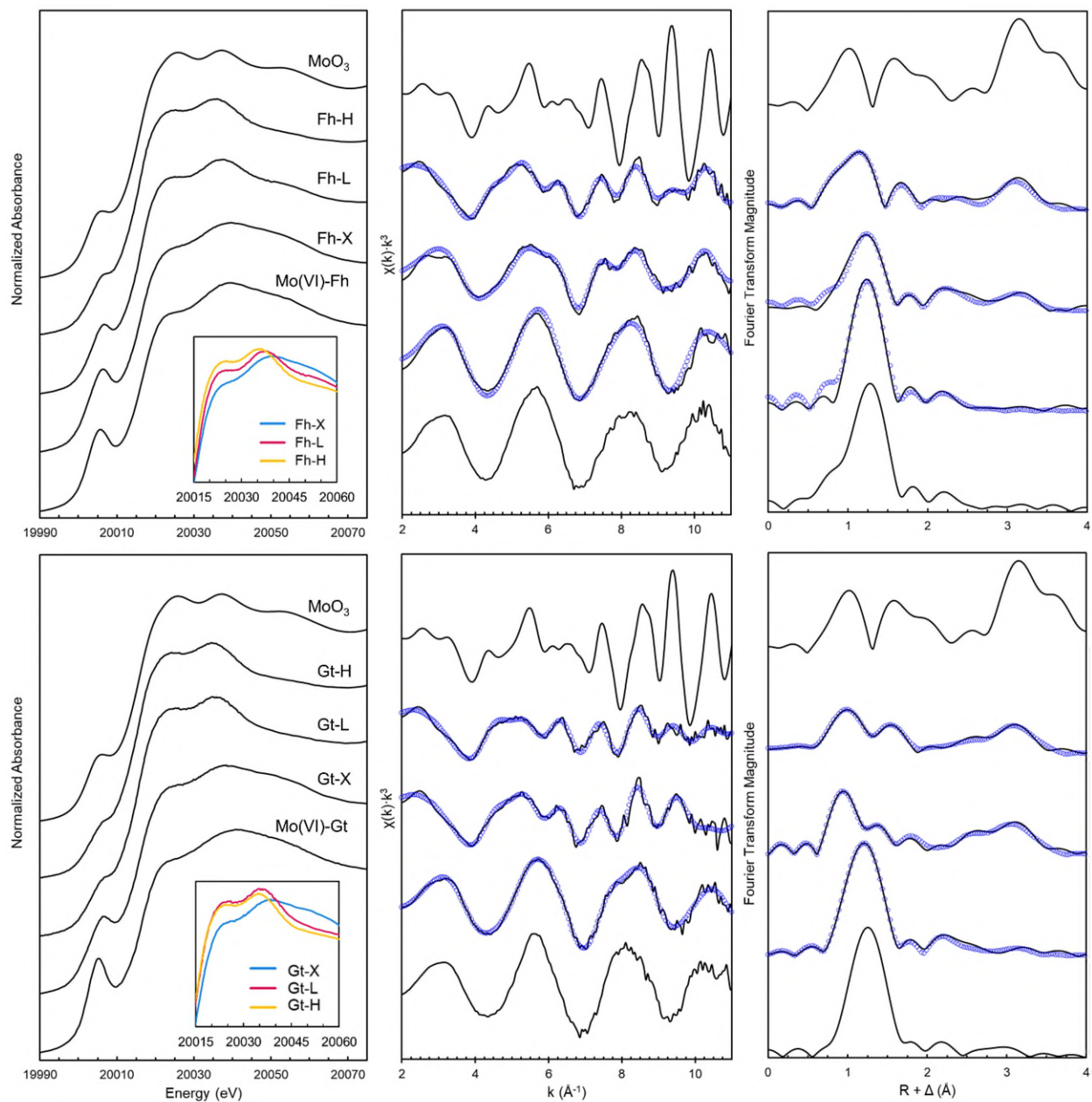
Figure 5. Molybdenum XANES, Mo EXAFS (k-space), and Mo EXAFS (R-space) spectra of the goethite (Gt) and ferrihydrite (Fh) columns from left to right. Sample and line order is preserved in each panel. Insert: Control column (i.e. no Fe(II) addition) = blue, Low Fe(II) column = red, and High Fe(II) column = gold.

Table 1. Fitting parameters for Mo K-edge EXAFS modeling of solid-phase samples from the six columns. Parameters include coordination number (CN), interatomic distance (R), and Debye-Waller factor (σ^2), amplitude reduction factor (S_0^2), energy shift (ΔE_0), and R-factor.

Shell	Parameter	Goethite			Ferrihydrite		
		Control	Low Fe(II)	High Fe(II)	Control	Low Fe(II)	High Fe(II)
Mo-O$_1$	CN	4	2.5(5)	2.0(4)	4	4	3.2
	R (Å)	1.736(6)	1.79(3)	1.80(3)	1.750(6)	1.79(2)	1.81(2)
	σ^2 (Å^2)	0.003	0.006	0.060	0.0039(9)	0.006	0.006
Mo-O$_2$	CN	---	3.0(6)	3.2(5)	---	1.2(6)	2.8
	R (Å)	---	2.00(4)	2.02(3)	---	2.05(5)	2.04(2)
	σ^2 (Å^2)	---	0.006	0.006	---	0.006	0.006
Mo-Mo	CN	---	1.7(5)	1.0(5)	---	0.6(8)	0.7(7)
	R (Å)	---	2.42(3)	2.46(5)	---	2.57(7)	2.55(6)
	σ^2 (Å^2)	---	0.010	0.010	---	0.010	0.010
Mo-Fe$_1$	CN	1.1(5)	2.6(6)	1.9(6)	0.5(6)	1(1)	0.4(7)
	R (Å)	2.72(3)	2.82(3)	2.82(3)	2.77(3)	2.78(8)	2.84(6)
	σ^2 (Å^2)	0.010	0.010	0.010	0.006	0.010	0.010
Mo-Fe$_2$	CN	1.1(3)	5.2(8)	4.6(8)	---	3(1)	4(1)
	R (Å)	3.48(2)	3.58(3)	3.59(3)	---	3.59(3)	3.58(2)
	σ^2 (Å^2)	0.010	0.010	0.010	---	0.010	0.010
	S_0^2	0.73(4)	0.75	0.75	0.85(8)	0.8(2)	0.8(1)
	ΔE_0	-5(1)	1(4)	3(4)	-3(1)	0(3)	-1(2)
	R-factor	0.0054	0.018	0.022	0.01	0.0176	0.028

For Table of Contents Only